POTSDAM-INSTITUT FÜR KLIMAFOLGENFORSCHUNG

Chaos
An Interdisciplinary Journal of Nonlinear Science

RESEARCH ARTICLE | OCTOBER 17 2023

Exploring the intensity, distribution and evolution of teleconnections using climate network analysis

Special Collection: Nonlinear dynamics, synchronization and networks: Dedicated to Jürgen Kurths' 70th birthday

Shang Wang ; Jun Meng ; Jingfang Fan

Chaos 33, 103127 (2023)
https://doi.org/10.1063/5.0153677

Exploring the intensity, distribution and evolution of teleconnections using climate network analysis

Cite as: Chaos 33, 103127 (2023); doi: 10.1063/5.0153677
Submitted: 11 April 2023 · Accepted: 1 September 2023 ·
Published Online: 17 October 2023

Shang Wang,[1] Jun Meng,[2,3] and Jingfang Fan[1,3,a)]

AFFILIATIONS

[1]School of Systems Science/Institute of Nonequilibrium Systems, Beijing Normal University, Beijing 100875, China
[2]School of Science, Beijing University of Posts and Telecommunications, Beijing 100876, China
[3]Potsdam Institute for Climate Impact Research, Potsdam 14412, Germany

Note: This paper is part of the Focus Issue on Nonlinear dynamics, synchronization and networks: Dedicated to Juergen Kurths' 70th birthday.

[a)]**Author to whom correspondence should be addressed:** jingfang@bnu.edu.cn

ABSTRACT

Teleconnections refer to long-range climate system linkages occurring over typically thousands of kilometers. Generally speaking, most teleconnections are attributed to the transmission of energy and propagation of waves although the physical complexity and characteristics behind these waves are not fully understood. To address this knowledge gap, we develop a climate network-based approach to reveal their directions and distribution patterns, evaluate the intensity of teleconnections, and identify sensitive regions using global daily surface air temperature data. Our results reveal a stable average intensity distribution pattern for teleconnections across a substantial spatiotemporal scale from 1948 to 2021, with the extent and intensity of teleconnection impacts increasing more prominently in the Southern Hemisphere over the past 37 years. Furthermore, we pinpoint climate-sensitive regions, such as southeastern Australia, which are likely to face increasing impacts due to global warming. Our proposed method offers new insights into the dynamics of global climate patterns and can inform strategies to address climate change and extreme events.

Teleconnections have been associated with global climate change and the occurrence of extreme events. However, accurately predicting their intensity remains a challenging task, necessitating a comprehensive understanding of the underlying physical mechanisms and complex interactions among various climate variables. In this study, we introduce a novel approach for assessing the intensity, distribution patterns, and propagation directions of teleconnections based on daily mean near-surface air temperature data and a series of dynamical and physical climate networks with time delay. Our method allows for the identification of sensitive regions and lays the groundwork for research and decision-making related to global warming, tipping points, air pollution, and extreme events linked to global climate change. Consequently, this improves our comprehension of the Earth's climate system and can inform effective climate change mitigation and adaptation strategies.

I. INTRODUCTION

The Earth is a complex system consisting of two main components, the ecosphere and the human factor, which interact nonlinearly, giving rise to feedback loops and emergent behaviors.[1,2] The complexity of the Earth's system arises from the intricate and often unpredictable interactions between these components.

Climate teleconnections play a crucial role in the Earth's complex climate system by describing persistent relationships between climate anomalies in geographically separated regions within both the atmosphere and ocean.[3–9] Teleconnections exist in both the atmosphere and the ocean and dominate climate change at different temporal and spatial scales.[3,10–12] Teleconnections have garnered significant attention due to their role in energy transport and global-scale climate dynamics occurring over typically thousands of kilometers. These patterns represent preferred modes of large-scale variability, and various methods have been developed to

capture them.[4,13–15] However, the mechanisms of specific teleconnections are not yet well understood, and there is a lack of a general method for determining their distribution patterns and intensity characteristics.

Among these teleconnection patterns, Rossby waves are particularly important due to their significant influence on climate phenomena, extreme weather events, air pollution, and the transport and distribution of CO_2.[8,16–20] Rossby waves operate primarily at mid-high latitudes and interact closely with numerous climate patterns, such as the Arctic Oscillation, the North Atlantic Oscillation, the El Niño-Southern Oscillation, and the North Pacific Oscillation-West Pacific pattern,[4,21–25] and have a relatively large dominant role in climate teleconnections and can pose a substantial safety risk to human life and property.[3]

There have been research[13,14] that comprehensively analyze the links between atmospheric rossby waves from different altitudes and climate variables such as air temperature, sea level pressure, geopotential height, and meridional velocity reanalysis fields. They capture the waves' properties also using other fields at various altitudes, showing that the Rossby waves' pattern is clearly seen at a ground level (1000 hPa) temperature field, a more common and reliable variable.[13] Previous studies found the 300 hPa meridional velocity field to be the most suitable for studying the characteristics of Rossby waves,[26–28] while the temperature field yields a clearer pattern at the ground level of 1000 hPa.[13] Meanwhile, the time delays observed over these long distances align with the direction of energy transport and the group velocity of atmospheric Rossby waves, and the prominent length scales, Southern Hemisphere dominance, and prevalence during Southern Hemisphere summer exhibited by the climate network are all consistent with the properties of these waves.[13] All of these factors, thus, provide strong support for the association of the majority of the climate network far links with Rossby waves.[13] The atmospheric temperature field is indeed influenced by many other factors, such as adiabatic processes on land and sea. But as mentioned above, there are plenty of reasons and confidences that these results are caused by atmospheric Rossby waves dominance, though perhaps indeed not entirely by them. Therefore, studying teleconnections and intensity characteristic is crucial to help us better understand Rossby waves and cope with the effects of climate change.

In recent years, statistical physics and network science[29–45] has emerged as a powerful tool in climate science.[38] Climate networks represent a unique approach to analyze climate data by constructing networks where the geographical locations of climate data points are considered network nodes, and the level of similarity between the data points determines the network links or edges.[46–50] Indeed, recurrence networks, as introduced by Donner *et al.*,[51] represent a distinctive approach where states are nodes, and edges are determined by similarities between states. This method can provide significant insights into both the dynamical properties of a process and the identification of teleconnection patterns, as demonstrated by Mukhin.[52] This approach has been successful in modeling and predicting climate phenomena, including extreme weather events, and can provide valuable insights into the underlying processes that drive climate variability and change.[8,18,33,38,40,48,53–66] As such, climate networks offer a promising avenue for advancing our understanding of Earth's complex climate system.[38,67]

In this study, we conduct a climate network analysis to reveal the distribution patterns and intensity characteristics of teleconnections. By exploring their complexity and potential impacts on climate mode, we aim to gain a better understanding of Earth's complex climate system and provide insights into assessing the safety risks associated with teleconnections.

II. DATA

Our climate network is based on the National Center for Environmental Prediction/National Center for Atmospheric Research (NCEP/NCAR) reanalysis daily surface or near the surface (0.995 sigma level) air temperature datasets, which are available at https://www.esrl.noaa.gov/psd/data/gridded/data.ncep.reanalysis.surface.html. The data have a spatial (zonal and meridional) resolution of $2.5^\circ \times 2.5^\circ$, resulting in $144 \times 73 = 10\,512$ grid points. The dataset covers a time period of 74 years, spanning from January 1948 to December 2021. The 500 hPa temperature and geopotential height data at the same spatiotemporal scale are also used, which are available at https://downloads.psl.noaa.gov/Datasets/ncep.reanalysis/Dailies/pressure/.

III. METHOD

A. Data preprocessing

To mitigate the strong effect of seasonality, we subtract the calendar day's mean from the time series of each node (in leap years, we exclude February 29; thus, all years have the same length). For each node i, with the temperature time series $T_i(d, y)$, $d = 1, 2, \ldots, 365$, $y = 1, 2, \ldots, 74$, we obtain the last using data $T_i(t)$, $t = 1, 2, \ldots, L = 74 \times 365$ by subtracting the mean value of each calendar's day and dividing by the standard deviation,

$$T_i(t) = RD\left(\frac{T_{i,d}(y) - Mean_{i,d}(y)}{SD_{i,d}(y)}\right), \tag{1}$$

where $T_{i,d}(y)$ is the temperature for a given selected point i, specific day d of the year y, $Mean_{i,d}(y) = \sum_{y=1}^{y=74} T_{i,d}(y)/Y$, and $SD_{i,d}(y) = \sqrt{\sum_{y=1}^{y=74} (T_{i,d}(y) - Mean_{i,d}(y))^2/Y}$. The step of dividing by the standard deviation aims to accommodate the fact that temperature fluctuations in the Northern and Southern Hemispheres differ and exhibit distinct variations. By implementing this step, we normalize the data from both hemispheres, enabling us to conduct our analysis and make comparisons using a unified standard scale. This normalizing procedure ensures that our subsequent network construction does not inadvertently favor one hemisphere over the other due to inherent differences in their seasonal temperature fluctuations.

To simplify subsequent calculations, we utilize a dimensionality reduction function, RD, to convert the two-dimensional year-day data $T_i(d, y)$ into one-dimensional day data $T_i(t)$. In order to reduce computational time complexity and address practical constraints, we selected 6570 points using a distance function and mapped them to the global network.[68] We define the resolution (in degree latitude) at the Equator as x_0 and calculate the number of nodes at the equator, $n_0 = 360/x_0$. For each latitude $x_0 l$, the number of nodes is $n_l = n_0 cos(x_0 l)$, where $l \in [-90/x_0, 90/x_0]$. The total number of nodes is $N = \sum_{l=0}^{l=90/x_0} 2n_l - n_0$. Here, we choose x_0 to be 2.5°, which

yields $N = 6570$. This resulted in the selection of a two-dimensional (L,6570) matrix to represent $\widetilde{T}_i(t)$. In order to eliminate the influence of enhanced land warming compared to the ocean surface, we have also removed long-term thermodynamic trends in our analysis. By detrending the data, we aim to focus on the variations and patterns that are not solely driven by long-term trends but are more indicative of the specific atmospheric dynamics, including Rossby wave teleconnections.

B. Climate network characteristics

To construct climate networks, we use the cross-correlation function with time lags to capture the interactions between different points. The detailed procedure is as follows: For each pair of nodes (climate points) i and j, we calculate the cross-correlation function $C_{i,j}(\tau)$ between $\widetilde{T}_i(t)$ and $\widetilde{T}_j(t)$, where $\tau = -\tau_{\max}, \ldots, \tau_{\max}$ represents the time lag. Here, for $\tau \geq 0$, $C_{i,j}(\tau)$ is defined as

$$C_{i,j}(\tau) = \frac{\left\langle \left(\widetilde{T}_i(t-\tau) - \overline{T_i}\right)\left(\widetilde{T}_j(t) - \overline{T_j}\right)\right\rangle}{\sqrt{\left\langle \left(\widetilde{T}_i(t-\tau) - \overline{T_i}\right)^2\right\rangle}\sqrt{\left\langle \left(\widetilde{T}_j(t) - \overline{T_j}\right)^2\right\rangle}}, \tag{2}$$

and for $\tau < 0$,

$$C_{i,j}(\tau) = \frac{\left\langle \left(\widetilde{T}_i(t) - \overline{T_i}\right)\left(\widetilde{T}_j(t+\tau) - \overline{T_j}\right)\right\rangle}{\sqrt{\left\langle \left(\widetilde{T}_i(t) - \overline{T_i}\right)^2\right\rangle}\sqrt{\left\langle \left(\widetilde{T}_j(t+\tau) - \overline{T_j}\right)^2\right\rangle}}, \tag{3}$$

where $\overline{T_i}$ and $\overline{T_j}$ are the average of $\widetilde{T}_i(t)$ and $\widetilde{T}_j(t-\tau)$ over the time period $t = \tau + 1, \ldots, L$. Here, we chose $\tau_{\max} = 800$ (days).[14]

We demonstrate an example in Fig. 1 by using cross-correlation to analyze the relationship between two nodes in the climate network. And given any two points such as i and j, we can calculate the actual spatial distance $R_{ij}(km)$ between the two points on Earth. The location of the two nodes is indicated in Fig. 1(a) using red and dark orange lines, and their distance is approximately 6261 km. Figures 1(b) and 1(c) show the two time series and the cross-correlation function, respectively. The maximal correlation between the two nodes is found to be about $C_{i,j} \approx 0.188$ at a time lag of 2 days.

The positive link weight between nodes i and j can be defined as

$$W_{i,j}^{pos} = \frac{C_{i,j}^{\max} - mean(C_{i,j}(\tau))}{std(C_{i,j}(\tau))}, \tag{4}$$

while the negative link weight is defined as

$$W_{i,j}^{neg} = \frac{C_{i,j}^{\min} - mean(C_{i,j}(\tau))}{std(C_{i,j}(\tau))}. \tag{5}$$

Here, we identify the maximum and minimum of the cross-correlation function and denote the corresponding time lag as $\tau_{i,j}^{pos}$ and $\tau_{i,j}^{neg}$, respectively, where $C_{i,j}^{\max} = C_{i,j}\left(\tau_{i,j}^{pos}\right)$ and $C_{i,j}^{\min} = C_{i,j}\left(\tau_{i,j}^{neg}\right)$, and the "mean" and "std" are the mean and SD of the cross-correlation function, respectively. The sign of $\tau_{i,j}$ indicates the direction of each link, i.e., if $\tau_{i,j}^{pos} > 0$, the direction of the link is from i to j; otherwise, it is from j to i.[33] Note that links with $\tau = 0$ are excluded. Then, we can construct networks based on $C_{i,j}^{\max}$, $C_{i,j}^{\min}$ and $W_{i,j}^{pos}$, $W_{i,j}^{neg}$.

The adjacency matrix of a climate network is defined as

$$A_{i,j}^{pos} = \begin{cases} 1, & W_{i,j}^{pos} \geq w_t^{pos} \\ 0, & W_{i,j}^{pos} < w_t^{pos} \end{cases} \tag{6}$$

and

$$A_{i,j}^{neg} = \begin{cases} 1, & W_{i,j}^{neg} \leq w_t^{neg} \\ 0, & W_{i,j}^{neg} > w_t^{neg} \end{cases}, \tag{7}$$

where w_t^{pos} and w_t^{neg} are two thresholds obtained by a shuffle procedure; see details in Sec. III C. Then, we can define degree (D), correlation (C), and weight (W) of each node i to measure the

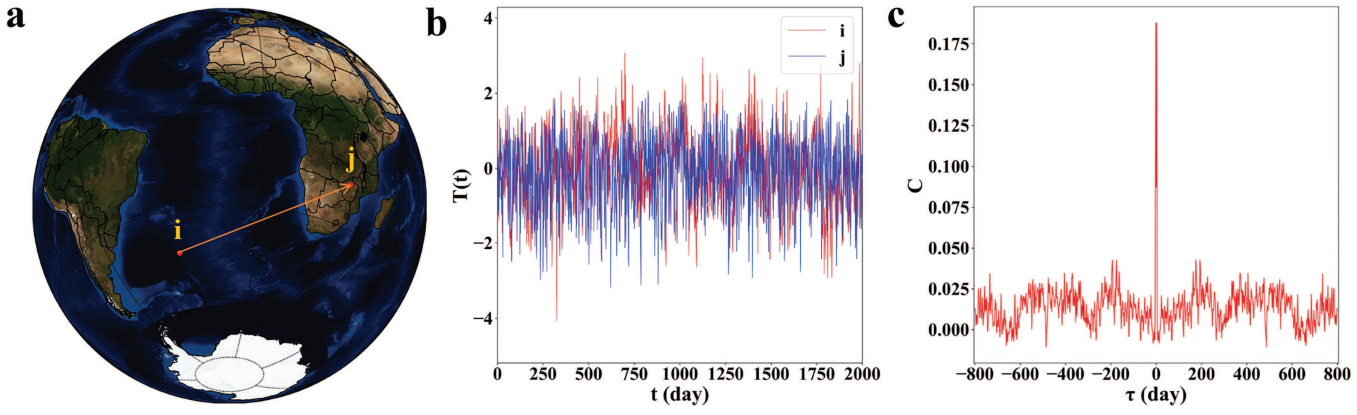

FIG. 1. Example of a link in the climate network. (a) The geographic locations of the two selected nodes, $i(-42.5^\circ$ S, 30° W) and $j(-17.5^\circ$S, 30°E). (b) The temporal evolutions of the temperature anomaly (in $^\circ$C) at these two points. (c) The cross-correlation function between the two time series, with a maximum correlation value of approximately 0.19 observed at a time lag of $\tau = 2$ days.

climate network characteristics,

$$D_i = \begin{cases} IND_i^{pos,neg} = \sum_{j\neq i} A_{i,j}^{pos,neg}, & if\ \tau_{i,j}^{pos,neg} < 0, \\ OUTD_i^{pos,neg} = \sum_{j\neq i} A_{i,j}^{pos,neg}, & if\ \tau_{i,j}^{pos,neg} > 0, \end{cases} \tag{8}$$

$$C_i = \begin{cases} INC_i^{pos,neg} = \sum_{j\neq i} A_{i,j}^{pos,neg} \cdot C_{i,j}^{pos,neg}, & if\ \tau_{i,j}^{pos,neg} < 0, \\ OUTC_i^{pos,neg} = \sum_{j\neq i} A_{i,j}^{pos,neg} \cdot C_{i,j}^{pos,neg}, & if\ \tau_{i,j}^{pos,neg} > 0, \end{cases} \tag{9}$$

$$W_i = \begin{cases} INW_i^{pos,neg} = \sum_{j\neq i} A_{i,j}^{pos,neg} \cdot W_{i,j}^{pos,neg}, & if\ \tau_{i,j}^{pos,neg} < 0, \\ OUTW_i^{pos,neg} = \sum_{j\neq i} A_{i,j}^{pos,neg} \cdot W_{i,j}^{pos,neg}, & if\ \tau_{i,j}^{pos,neg} > 0, \end{cases} \tag{10}$$

where $IND_i^{pos,neg}$ and $OUTD_i^{pos,neg}$ represent the in and out degrees of node i in positive and negative links, respectively. $INC_i^{pos,neg}$ and $OUTC_i^{pos,neg}$ represent the input and output correlations of node i in positive and negative links, respectively. $INW_i^{pos,neg}$ and $OUTW_i^{pos,neg}$ represent the input and output weights of node i in positive and negative links, respectively.

In the context of our climate network, the in-degree of a node represents the number of other nodes (locations) that significantly influence the climate of the node in question. Conversely, the out-degree represents the number of nodes (locations) that the node in question significantly influences. These degrees serve as fundamental measures in the network analysis, helping us to identify key areas in the global climate system based on the extent of their influences and their susceptibility to influences from others.

Then, we construct the climate network using the geographic location of the actual space as nodes and significant weight W as edges, and the direction of each edge depends on the respective time delay τ. The same can be done for correlation C to construct the climate network. In turn, we can calculate the indexes for each node in the network using the above method.

C. Significance tests

In this study, we utilize a shuffling procedure to assess the significance of link weights in the surrogate case. The procedure involves randomly shuffling the two time series $\widetilde{T}_i(t)$ and $\widetilde{T}_j(t)$ for each pair of nodes i and j, with t spanning 74 years. We calculate a control threshold based on the shuffled network weights, and any link weight in the original network that surpasses this threshold is considered significant or reliable, whereas link weights below the threshold are considered spurious. The explanation of this procedure is shown in Figs. 2(a) and 2(b). The shuffling procedure plays a crucial role in the analysis of climate networks as it allows us to distinguish between meaningful and spurious correlations. By comparing the original link weights with those obtained from shuffled data, we can assess the statistical significance of the relationships within the network. This process helps to filter out random correlations that may arise by chance, providing a more reliable and accurate representation of the underlying climatic dynamics.

In addition, we also incorporate the yearly shuffling method, which retains the original order of data within each year but randomizes the order of the years themselves. This approach allows us to maintain the annual-scale evolution patterns while disrupting the correlations between different years.[69] By comparing and analyzing the results obtained from both daily shuffling and yearly shuffling procedures, as shown in Figs. 2 and S1, we are able to assess the impact of data noise and identify more significant weight thresholds.

IV. RESULTS AND DISCUSSION

A. Climate network properties analysis

It is essential to recognize that the statistical analysis of the four variables (distance, cross-correlation, weight, and time delay) is performed for both the original and shuffled data. This approach enables the identification of significant links in the climate network and assists in differentiating between real and spurious links. The results of the analysis are presented in Figs. 2(a) and 2(b) as well as in the SI Appendix, Figs. S2–S4. This analysis offers valuable insights into the relationships among the variables and their influence on the network structure. By examining the statistics of these variables, it becomes possible to pinpoint key factors that affect the formation and strength of links within the climate network.

Figure 2 showcases the statistical relation analysis between the variables of distance (R) and weight (W) for both original and shuffled data. Figure 2(a) reveals that geographic locations in close proximity ($R < 2000$ km) tend to have a strong positive correlation, attributed to adjacent spatial auto-correlation. However, for the positive link weight (W^{pos}), a peak is observed at $R \sim 7000$ km, corresponding to the physical distance of one wavelength of atmospheric Rossby waves.[13,14,19] Figure 2(b) illustrates that for the negative link weight (W^{neg}), there are two peaks. The first peak occurs at $R \sim 3500$ km, and the second peak is found at $R \sim 10000$ km, corresponding to the 1/2 and 3/2 wavelength of the atmospheric Rossby waves.[13,14] These findings suggest that our climate correlation networks can detect some imprints of atmospheric Rossby wave patterns.[13,14]

Additional results can be found in the supplementary material. Specifically, Fig. S2(a) in the supplementary material demonstrates that $C_{i,j}^{\max}$ declines gradually as R increases. This pattern is similar to the one observed for $W_{i,j}^{pos}$ with respect to R, where $C_{i,j}^{\max}$ exhibits a proximity effect at short distances. However, it does not display the same convex hull at a distance of 7000 km. Meanwhile, Fig. S2(b) in the supplementary material illustrates the relationship between $C_{i,j}^{\min}$ and $R(km)$, indicating that $C_{i,j}^{\min}$ is not highly sensitive to changes in distance. Moreover, the relationship between $W_{i,j}$ and τ is explored in Figs. S3(a) and (b) in the supplementary material. These figures reveal that most high-weight values have relatively short propagation times, peaking at 15 days. The propagation time for high-weight connections within short distances (less than 2000 km) does not exceed 3 days. However, for Figs. S2(c) and (d) in the supplementary material, the relationship between $C_{i,j}$ and τ does not exhibit a clear pattern, except for a peak at $\tau = 0$.

Further analysis of the scatter diagrams of $C_{i,j}^{\max}$—$W_{i,j}^{pos}$ and $C_{i,j}^{\min}$—$W_{i,j}^{neg}$ reveals an obvious "V" shape and an inverted "V" shape, respectively. When the absolute value of $W_{i,j}$ is small ($W_{i,j} < 5$),

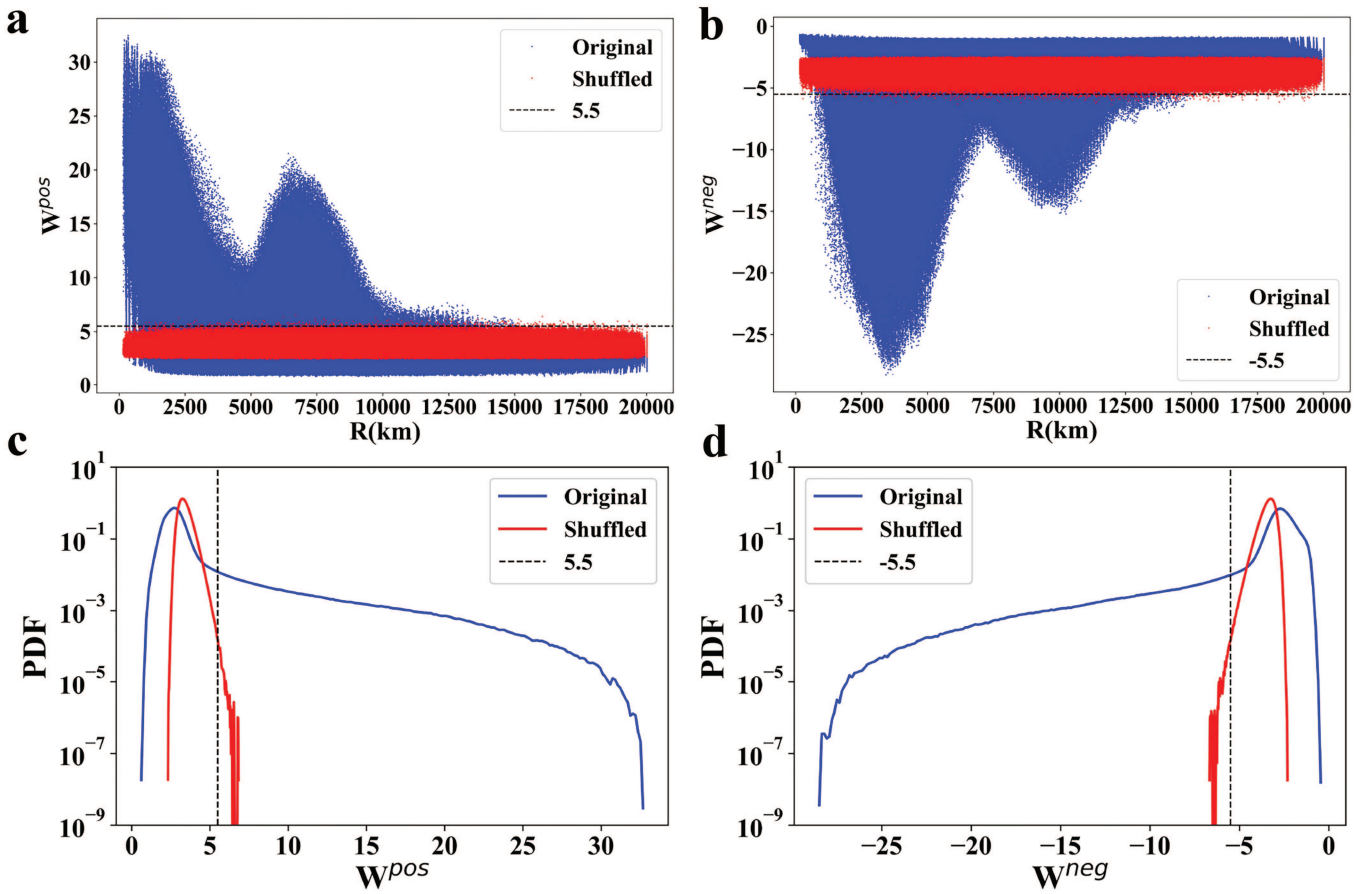

FIG. 2. Mining of teleconnection links in the climate networks.[13,14] (a) Positive link weights W^{pos} as a function of geographical distances R for both observed (blue) and shuffled (red) data. (b) Negative link weights W^{neg} as a function of geographical distances R for both Original (blue) and shuffled (red) data. (c) The probability density function (PDF) of positive link weights shown in (a). (d) Analogue to (c) but for negative links. The dashed horizontal or vertical lines in each panel indicate the strength of the threshold ($W_t^{pos} = 5.5$ and $W_t^{neg} = -5.5$), i.e., more than the lower (higher) bound of the top (bottom) 5% links, which is also higher than the 95% confidence level of the randomly shuffled links.

$C_{i,j}$ can change greatly and even reach its absolute maximum value. As the absolute value of $W_{i,j}$ increases, $C_{i,j}$ and $W_{i,j}$ become more strongly linearly related. These findings suggest that $W_{i,j}$ is a more suitable indicator for measuring the intensity of connection weights than $C_{i,j}$. Please see the diagram of Fig. S4 in the supplementary material for details.

In order to eliminate the noise influence of the data itself as much as possible, we synthesized and analyzed the maximum top 5% thresholds of the two shuffled methods (daily shuffling and yearly shuffling), combined with the $W_{i,j}$—R graphs, and finally decided to choose $w_t^{pos} = 5.5$ and $w_t^{neg} = -5.5$ as our thresholds, which can be referred to Fig. S1 in the supplementary material. As can be clearly found that $w_t^{pos} = 5.5$ and $w_t^{neg} = -5.5$ thresholds are both significantly higher than the 95% confidence level.

In Figs. 2(c) and 2(d), we present the probability density function (PDF) of $W_{i,j}^{pos}$ and $W_{i,j}^{neg}$, respectively, with respect to distance R. We also calculate the results with limits of $R > 5000$ km for positive weights and $R > 7000$ km for negative weights, as shown in Fig. S5 in the supplementary material. These links we called teleconnections. We find that the distribution results are robust.[13,14,19]

B. Intensity distribution characteristics of teleconnections

In the following, we focus on the teleconnections with large weights ($R > 5000$ km for positive and $R > 7000$ km for negative). Figure 3 provides an illustration of the distribution and intensity patterns of IN Weight (INW) and OUT Weight (OUTW) for positive and negative global teleconnections, which agree well with the regions affected by Rossby waves in middle and high latitudes.[13,27,28] In Figs. 3(a) and 3(c), the darker the color red/blue, the greater the positive/negative impact on the area. Conversely for Figs. 3(b) and 3(d), the darker the red/blue color, the greater the positive/negative influence of the area on the outside world. In view of

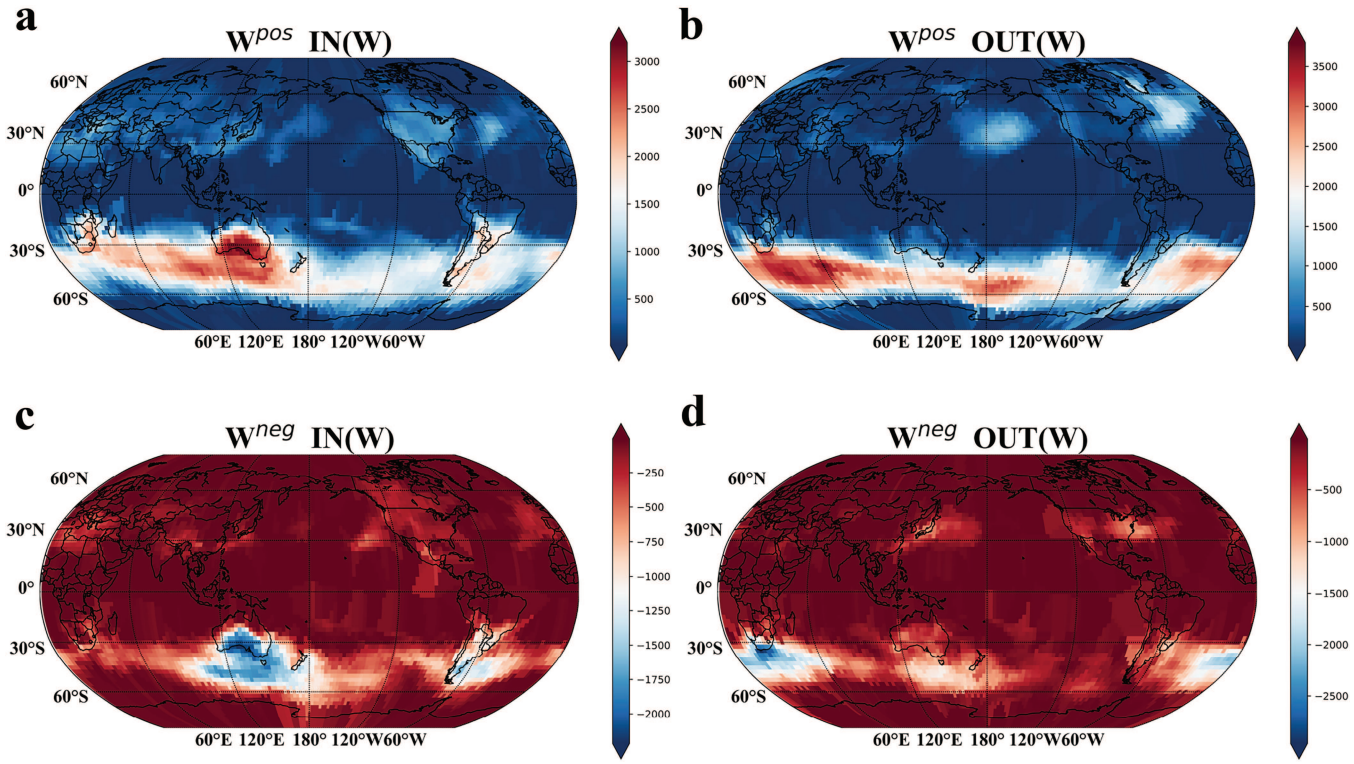

FIG. 3. The intensity distribution of teleconnections in the climate network. (a) $IN(W)$ of positive links; (b) $OUT(W)$ of positive links; (c) $IN(W)$ of negative links; and (d) $OUT(W)$ of negative links.

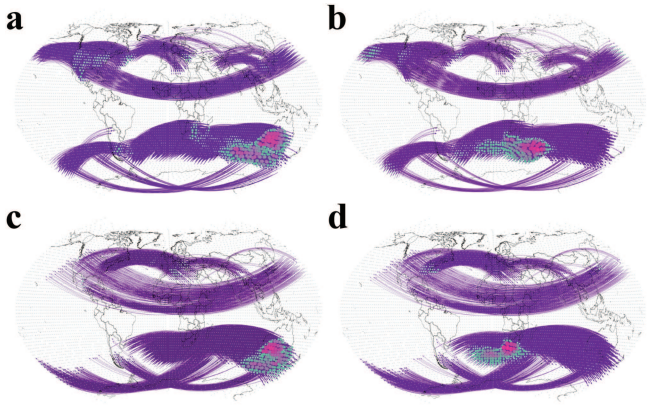

FIG. 4. The teleconnections structure in the climate network. Top 5% of positive links for (a) nodes with in-degree pattern and (b) nodes with out-degree pattern. Top 10% of negative (absolute) links for (c) nodes with in-degree pattern and (d) nodes with out-degree pattern. Node size/color represents the value of degrees. The top 5% and 10% thresholds were chosen for better visualization.

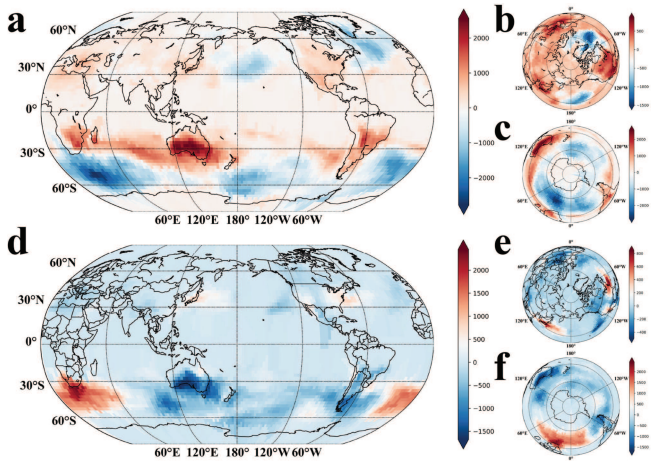

FIG. 5. The divergence of teleconnections intensity spatial pattern. (a) For the positive links, INW_i^{pos} - $OUTW_i^{pos}$. (b) and (c) show the same information as (a) but viewed from the perspective of the North and South Pole. (d) For the negative links, INW_i^{neg} - $OUTW_i^{neg}$. (e) and (f) show the same information as (d) but viewed from the perspective of the North and South Pole.

the degree differences between the Northern and Southern hemispheres, a view of the Northern Hemisphere is supplemented in Appendix Fig. S6 in the supplementary material.

Our analysis shows that the intensities of both *INW* and *OUTW* are considerably higher in the Southern Hemisphere (SH) compared to the Northern Hemisphere (NH), indicating that teleconnections in the SH are more stable and prominent. This may be attributed to the fact that the NH has more complex terrain, environmental pollution, forest fires caused by human activities, and the cascading Arctic amplification effect, leading to the influence of teleconnections and Rossby waves is more and more instability and rapid changes.[70] Conversely, the majority of the SH consists of oceans, which contribute to more stable teleconnections and Rossby waves' formation.[26–28,71,72]

Furthermore, the distribution of both $INW_{i,j}^{pos}$ and $INW_{i,j}^{neg}$ tends to be concentrated on land, particularly in Europe-Africa, East Asia, and the United States in the NH as well as South Australia, South Africa, and South America in the SH.[13] In contrast, the distribution of $OUTW_{i,j}^{pos}$ and $OUTW_{i,j}^{neg}$ tends to be concentrated on oceans, particularly in the Northern Pacific Ocean, Southern Greenland Ocean (North Atlantic) in the NH, and the ocean areas in the southeast of Africa, southeast of Australia, and southeast of America in the SH.[13] These findings shed light on the role of land and oceans in modulating teleconnections.

Figure S7 in the supplementary material presents the results for IN degree (IND) and OUT degree (OUTD) fields, which have similar distribution characteristics.[13] In the context of this study, we leverage the concept of "degree" in a network to indicate the number of connections a node has. When dealing with a climate network, where nodes represent geographical locations and edges represent teleconnections, the degree of a node represents its connectivity or influence with other nodes in the network. In terms of spatial propagation, a high degree node would suggest that changes in the state of that node have a wider influence. Hence, if we visualize the network in a spatial context, such a node would be the "source" of a spatial propagation of effects to other nodes (regions). So we can delimit sub-regions and analyze the incoming and outgoing edges separately to obtain the global teleconnections that influence the direction. By applying this method, we are able to mine the propagation directions

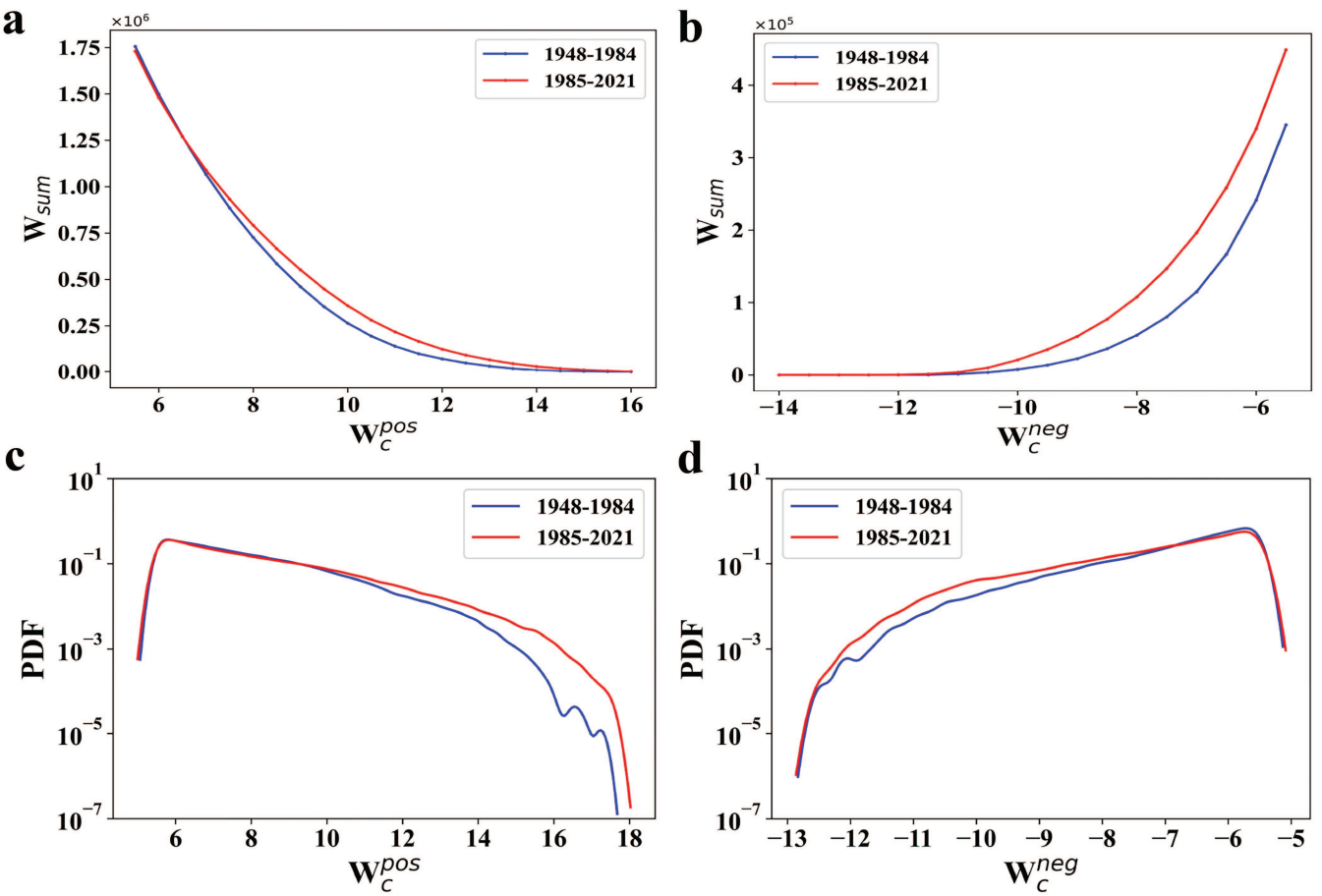

FIG. 6. Cumulative weight strength W_{sum} of (a) positive and (b) negative teleconnections as a function of threshold W_c^{pos}/W_c^{neg} for the first 37 years 1948–1984 (blue) and the last 37 years 1985–2021 (red). The probability density function (PDF) of link (c) positive and (d) negative weights.

of global teleconnections, which are shown in Fig. 4, and are consistent with the directions of planetary Rossby waves.[13] The view of the NH is supplemented in Appendix Fig. S8 in the supplementary material.

Considering the intensity differences between the northern and southern hemispheres, we also have built, calculated, and analyzed separate networks for the northern and southern hemispheres as well as the equatorial region, and the results can be found in Figs. S14–S16 in the supplementary material. We discover that the results of building a separate network were consistent with the previous results, which mirrored the correctness of our previous results. And the display of the results at the equatorial region shown in Fig. S16 is insignificant. This is consistent with the understanding that atmospheric Rossby waves primarily manifest in the mid-latitudes rather than near the equator. The limited impact observed at the equatorial region aligns with the characteristic behavior of Rossby waves, further supporting our findings.

We then analyze the global teleconnections by examining the divergence of *INW* and *OUTW* for both positive and negative cases, as depicted in Fig. 5, and the divergence for degree is shown in Fig. S9 in the supplementary material. The alternating pattern of teleconnections, propagating mainly from west to east, high latitude to mid-latitude, is clearly displayed in red and blue patterns and very similar to Rossby waves.[13,14,16] Specifically, three alternating red–blue phase distribution patterns correspond to six half-wavelengths or three to four full wavelengths. Considering that our results are averaged over a substantial spatial and temporal scale of 74 years, the patterns and intensity characteristics of teleconnections they display are indeed stable and robust. It is noteworthy that these characteristics observed in our analysis are distinct from those of waves that operate on shorter time scales. These short-term waves tend to change rapidly within a span of hours and exhibit recurrent movement around the Earth's atmospheric cycle, resulting in their inherent instability. In contrast, the teleconnection patterns associated with Rossby waves, as identified in our study, operate on longer time scales and display more persistent and stable behavior. These differences highlight the unique nature of Rossby waves and their impact on global climate dynamics.

Similarly, considering the influence of other effects such as sea–land adiabatic processes, we also apply the method to the 500hpa temperature field and obtain the same similar results, see Figs. S17–S22 in the supplementary material. It shows that indeed atmospheric Rossby waves play a very important dominant role for teleconnections, and our analysis and results are reliable. And results for 500 hpa geopotential height are shown in Figs. S23–S24 in the supplementary material. And we also calculate the similar and robust results for different thresholds by top 5% shuffled. Our findings provide valuable insights into the stable and reliable features of teleconnections, contributing to a better understanding of atmospheric dynamics.

C. The spatiotemporal evolutions of teleconnections

To analyze the evolutions of strength patterns over time, we apply the aforementioned method to calculate the strength patterns for two different periods: the first 37 years (1948–1984) and the last 37 years (1985–2021). The resulting $W_{i,j}$—$D_{i,j}$ values and their probability density functions (PDFs) are presented in Figs. S10 and S11 in the supplementary material, respectively. We examine the teleconnections in the climate network with the thresholds of $R > 5000$ km and $R > 7000$ km as well as $W_{i,j}^{pos} \geq 5.5$ and $W_{i,j}^{neg} \leq -5.5$. We then calculate the number of links and weight sum of edges for $W_{i,j}^{pos}$ and $W_{i,j}^{neg}$, respectively. Figure 6 displays the results of the difference in weight sum between the first 37 years and last 37 years. Moreover, we compute the increasing rate by subtracting the number or weight sum of the last 37 years from that of the first 37 years and dividing the first 37 years, as demonstrated in Fig. S12 in the supplementary material.

We find that as the selected threshold W_t increases, the teleconnections sum-weight of the last 37 years consistently exceeds that of the first 37 years for $W_{i,j}^{pos}$, and the increasing rate continues to rise for W_t^{pos} above 6.5, as shown in Fig. S12(a) in the supplementary material. On the other hand, for $W_{i,j}^{neg}$ as shown in Fig. S12(b) in the supplementary material, although the quantity and sum-weight of teleconnections show a persistent decrease, the increasing rate becomes much higher. When $W_t^{neg} \leq -6.5$, the significant weight of teleconnections added is more than half of that in the first 37 years.

These results suggest that for both positive and negative teleconnections with significant weight, the quantity of teleconnections is increasing over a large spatiotemporal scale, with the intensity of teleconnections showing an increasing trend over time. Although the spatial distance R remains constant for any teleconnection, the weight has increased. We further explore the specific regions that are influenced by teleconnections, and the results are presented in Figs. 7 and 8.

Figure 8 displays the spatiotemporal evolutions of the intensity transform pattern of teleconnections from 1948 to 2021, with threshold $W_t^{pos} = 5.5$ and $W_t^{neg} = -5.5$. The changes in the SH are notable, as evident from Fig. 8. For instance, the southern Indian Ocean is divided into two parts, where the positive output has

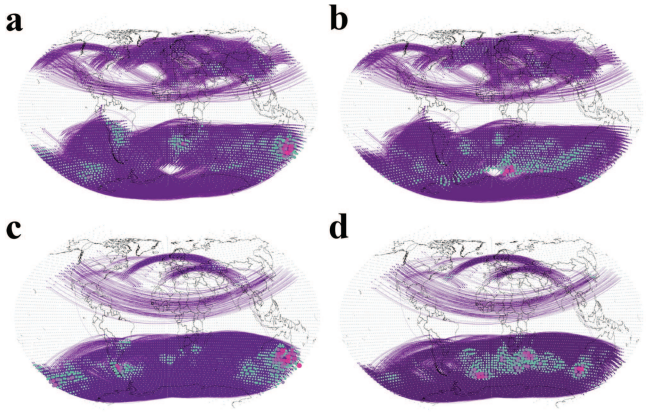

FIG. 7. The diagram of increased teleconnections in the global climate network. For positive and negative teleconnections, we separately select the top 50% of weight max for NH and SH. (a)$W_{i,j}^{pos}$ indegree. (b)$W_{i,j}^{pos}$ outdegree. (c)$W_{i,j}^{neg}$ indegree. (d)$W_{i,j}^{neg}$ outdegree. The node size and color represent the size of the node degree. The top 50% thresholds were chosen for better visualization.

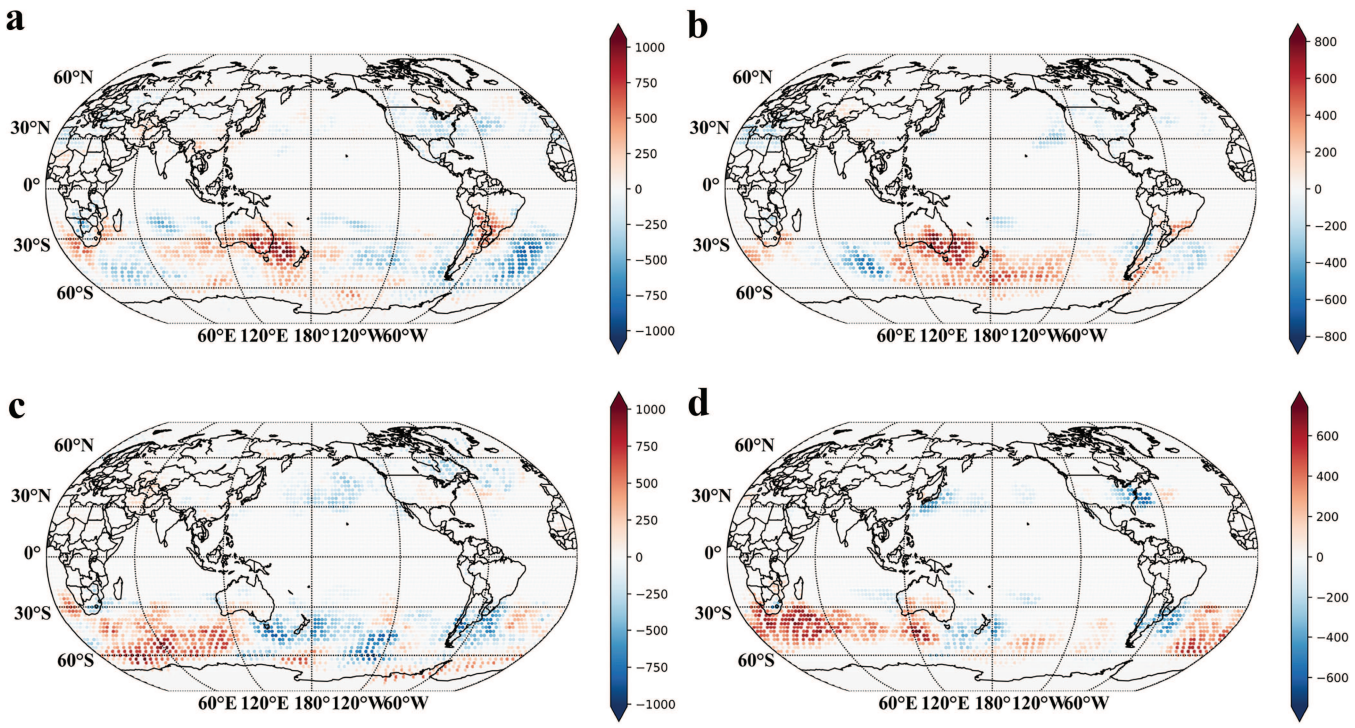

FIG. 8. The quantitative change of W_{ij} for positive and negative teleconnections between 1948–1984 and 1985–2021. (a) The divergence of INW_{ij}^{pos}. (b) The divergence of INW_{ij}^{neg}. (c) The divergence of $OUTW_{ij}^{pos}$. (d) The divergence of $OUTW_{ij}^{neg}$. The red colored nodes indicate the region with an increase in weight, and the blue area indicates a decrease. The results for D_{ij} are shown in Fig. S13.

increased substantially in one part (the southwestern oceans of Australia, near the South Pole), while the negative output has also increased considerably in the other part (the oceans in the southeast of Africa). This could suggest that the impact of teleconnections of the southern Indian Ocean on Australia and the surrounding ocean is intensifying. Regarding southeast Australia, the positive in-links are increasing, out-links are decreasing, negative in-links are increasing, and negative out-links are decreasing. These changes align with those observed in the South Indian Ocean. As a result, we hypothesize that this area will become progressively influenced by teleconnections in the future and may serve as a "hotspot" due to the reduction in both positive and negative outputs. This could contribute to the triggering of a tipping point event in the whitening of coral reefs in the Australian region.[73,74] Another noteworthy point in the SH is the symmetry and complementary in-links and out-links changes of the land and ocean in southern South America and southern Africa under large-scale interannual changes.

Regarding the NH, we find three relatively significant regions where the intensity of the teleconnection effect is weakening: the central part of the North Pacific and the northeastern part of the United States, the eastern part of the Asia and the western coast of the United States, and the junction of the northeastern part of the United States and the Eurasian continent. However, Fig. 8 also reveals that the positive impact of the North Atlantic on the Caspian Sea and the Qinghai-Tibet Plateau is enhanced, although the increased intensity is limited. Thus, the variation in teleconnection influence intensity in the NH is relatively stable and not apparent at a spatiotemporal scale spanning 74 years. We suspect that this stability is due to the combined effects of the changeable jet stream and complex geographical environment in the NH.

V. CONCLUSION

In this study, we examined the teleconnections mainly dominated by atmospheric Rossby waves using a climate network approach. Our framework enabled us to identify the direction and distribution characteristics of teleconnections on a global scale, revealing that "in-links" are concentrated on land (e.g., Europe, Africa, East Asia, and America in the NH, and South Africa, Australia, and South America in the SH), while "out-links" predominantly originate from the oceans.[13] We also quantitatively evaluated the intensity of teleconnections and found that it is significantly stronger and more stable in the SH than in the NH. This may be due to the complex geographical environment of the Northern Hemisphere, jet stream, human activities, and the cascading effects of climate tipping points over time.[26–28,71–73]

Our analysis of the divergence of the degree and weight of teleconnections reveals stable average intensity characteristics and

distribution patterns of teleconnections (waves 3–4) on large spatiotemporal scales spanning 74 years in mid-high latitudes. We established two layers of the global climate network on the temporal scale, based on the first 37 years (1948-1984) and the last 37 years (1985-2021), respectively, and comparatively analyzed the distribution pattern and intensity characteristics of teleconnections on these layers. We found that most of the teleconnections' intensities in the NH are slightly weakening, while the influence of the ocean in the SH on land is significantly increasing, forming several "hot spot" climate-sensitive areas (e.g., Southeastern Australia, Southern South America, and South Africa) between 1948–1984 and 1985–2021.[74] Furthermore, our analysis indicated that the intensity of teleconnections is increasing over time, which may be related to climate change, global warming, human activities, and the activation of climate tipping points.[73,74]

SUPPLEMENTARY MATERIAL

See the supplementary material for additional sources of data and data analysis that support the findings in the paper.

ACKNOWLEDGMENTS

We acknowledge the support by the National Natural Science Foundation of China (NSFC) (Grant Nos. 12275020, 12205025, and 12135003).

AUTHOR DECLARATIONS

Conflict of Interest

The authors have no conflicts to disclose.

Author Contributions

Shang Wang: Data curation (equal); Software (equal); Validation (equal); Visualization (equal); Writing – original draft (equal); Writing – review & editing (equal). **Jun Meng:** Conceptualization (equal); Methodology (equal); Supervision (equal); Writing – review & editing (equal). **Jingfang Fan:** Conceptualization (lead); Formal analysis (lead); Investigation (lead); Methodology (lead); Project administration (lead); Resources (lead); Supervision (lead); Writing – original draft (lead); Writing – review & editing (lead).

DATA AVAILABILITY

The data that support the findings of this study are openly available in NOAA at https://psl.noaa.gov/thredds/catalog/Datasets/ncep.reanalysis/Dailies/surface/catalog.html, Ref. 75 and in NOAA at https://downloads.psl.noaa.gov/Datasets/ncep.reanalysis/Dailies/pressure/, Ref. 75.

REFERENCES

[1]H. J. Schellnhuber, "'Earth system' analysis and the second Copernican revolution," Nature **402**, C19–C23 (1999).
[2]W. Steffen, K. Richardson, J. Rockström, H. J. Schellnhuber, O. P. Dube, S. Dutreuil, T. M. Lenton, and J. Lubchenco, "The emergence and evolution of earth system science," Nat. Rev. Earth Environ. **1**, 54–63 (2020).
[3]Y. Li, W. Lu, H. Xiao, S. Zhang, and Y. Li, "Dip-scanning coherence algorithm using eigenstructure analysis and supertrace technique," Geophysics **71**, V61–V66, https://doi.org/10.1190/1.2194899 (2006).
[4]S. Nigam and S. Baxter, "General circulation of the atmosphere—Teleconnections," in *Encyclopedia of Atmospheric Sciences*, 2nd edition, edited by G. R. North, J. Pyle, and F. Zhang (Academic Press, 2015), pp. 90–109.
[5]J. Bjerknes, "Atmospheric teleconnections from the equatorial pacific," Mon. Weather Rev. **97**, 163–172 (1969).
[6]J. M. Wallace and D. S. Gutzler, "Teleconnections in the geopotential height field during the northern hemisphere winter," Mon. Weather Rev. **109**, 784–812 (1981).
[7]H. Von Storch and F. W. Zwiers, *Statistical Analysis in Climate Research* (Cambridge University Press, 2002).
[8]N. Boers, B. Goswami, A. Rheinwalt, B. Bookhagen, B. Hoskins, and J. Kurths, "Complex networks reveal global pattern of extreme-rainfall teleconnections," Nature **566**, 373–377 (2019).
[9]Y. Mao, Y. Zou, L. M. Alves, E. E. N. Macau, A. S. Taschetto, A. Santoso, and J. Kurths, "Phase coherence between surrounding oceans enhances precipitation shortages in northeast Brazil," Geophys. Res. Lett. **49**, e2021GL097647, https://doi.org/10.1029/2021GL097647 (2022).
[10]Z. Liu and M. Alexander, "Atmospheric bridge, oceanic tunnel, and global climatic teleconnections," Rev. Geophys. **45**(2), 1, https://doi.org/10.1029/2005RG000172 (2007).
[11]J. Kurths, A. Agarwal, R. Shukla, N. Marwan, M. Rathinasamy, L. Caesar, R. Krishnan, and B. Merz, "Unravelling the spatial diversity of indian precipitation teleconnections via a non-linear multi-scale approach," Nonlin. Process. Geophys. **26**, 251–266, https://doi.org/10.5194/npg-26-251-2019 (2019).
[12]A. Agarwal, L. Caesar, N. Marwan, R. Maheswaran, B. Merz, and J. Kurths, "Network-based identification and characterization of teleconnections on different scales," Sci. Rep. **9**, 8808 (2019).
[13]Y. Wang, A. Gozolchiani, Y. Ashkenazy, Y. Berezin, O. Guez, and S. Havlin, "Dominant imprint of rossby waves in the climate network," Phys. Rev. Lett. **111**, 138501 (2013).
[14]D. Zhou, A. Gozolchiani, Y. Ashkenazy, and S. Havlin, "Teleconnection paths via climate network direct link detection," Phys. Rev. Lett. **115**, 268501 (2015).
[15]J. Hlinka, D. Hartman, M. Vejmelka, D. Novotná, and M. Paluš, "Non-linear dependence and teleconnections in climate data: Sources, relevance, nonstationarity," Clim. Dynam. **42**, 1873–1886 (2014).
[16]V. Petoukhov, S. Rahmstorf, S. Petri, and H. J. Schellnhuber, "Quasiresonant amplification of planetary waves and recent northern hemisphere weather extremes," Proc. Natl. Acad. Sci. U.S.A. **110**, 5336–5341 (2013).
[17]H. Teng, G. Branstator, H. Wang, G. A. Meehl, and W. M. Washington, "Probability of US heat waves affected by a subseasonal planetary wave pattern," Nat. Geosci. **6**, 1056–1061 (2013).
[18]A. Agarwal, N. Marwan, R. Maheswaran, B. Merz, and J. Kurths, "Quantifying the roles of single stations within homogeneous regions using complex network analysis," J. Hydrol. **563**, 802–810 (2018).
[19]N. Ying, D. Zhou, Z. G. Han, Q. H. Chen, Q. Ye, and Z. G. Xue, "Rossby waves detection in the CO_2 and temperature multilayer climate network," Geophys. Res. Lett. **47**, e2019GL086507, https://doi.org/10.1029/2019GL086507 (2020).
[20]Y. Zhang, J. Fan, X. Chen, Y. Ashkenazy, and S. Havlin, "Significant impact of rossby waves on air pollution detected by network analysis," Geophys. Res. Lett. **46**, 12476–12485, https://doi.org/10.1029/2019GL084649 (2019).
[21]C. Deser, M. A. Alexander, S.-P. Xie, and A. S. Phillips, "Sea surface temperature variability: Patterns and mechanisms," Annu. Rev. Marine Sci. **2**, 115–143 (2010).
[22]H. A. Dijkstra, *Nonlinear Climate Dynamics* (Cambridge University Press, 2013).
[23]K. C. Mo and R. W. Higgins, "The pacific–south american modes and tropical convection during the southern hemisphere winter," Mon. Weather Rev. **126**, 1581–1596 (1998).
[24]A. Gershunov and T. P. Barnett, "Interdecadal modulation of ENSO teleconnections," Bull. Am. Meteorol. Soc. **79**, 2715–2726 (1998).

[25]M. A. Alexander, I. Bladé, M. Newman, J. R. Lanzante, N.-C. Lau, and J. D. Scott, "The atmospheric bridge: The influence of ENSO teleconnections on air–sea interaction over the global oceans," J. Clim. **15**, 2205–2231 (2002).
[26]E. K. M. Chang, "Downstream development of baroclinic waves as inferred from regression analysis," J. Atmos. Sci. **50**, 2038–2053 (1993).
[27]E. K. M. Chang and D. B. Yu, "Characteristics of wave packets in the upper troposphere. Part I: Northern hemisphere winter," J. Atmos. Sci. **56**, 1708–1728 (1999).
[28]E. K. M. Chang, "Characteristics of wave packets in the upper troposphere. Part II: Seasonal and hemispheric variations," J. Atmos. Sci. **56**, 1729–1747 (1999).
[29]D. J. Watts and S. H. Strogatz, "Collective dynamics of 'small-world' networks," Nature **393**, 440–442 (1998).
[30]A.-L. Barabási and R. Albert, "Emergence of scaling in random networks," Science **286**, 509–512 (1999).
[31]R. Cohen and S. Havlin, *Complex Networks: Structure, Robustness and Function* (Cambridge University Press, 2010).
[32]M. Newman, *Networks: An Introduction*, 1st ed. (Oxford University Press, 2010).
[33]J. Fan, J. Meng, Y. Ashkenazy, S. Havlin, and H. J. Schellnhuber, "Network analysis reveals strongly localized impacts of El Niño," Proc. Natl. Acad. Sci. U.S.A. **114**, 7543–7548 (2017).
[34]R. Albert and A.-L. Barabási, "Statistical mechanics of complex networks," Rev. Mod. Phys. **74**, 47–97 (2002).
[35]D. Brockmann and D. Helbing, "The hidden geometry of complex, network-driven contagion phenomena," Science **342**, 1337–1342 (2013).
[36]R. Pastor-Satorras, C. Castellano, P. Van Mieghem, and A. Vespignani, "Epidemic processes in complex networks," Rev. Mod. Phys. **87**, 925–979 (2015).
[37]F. Morone and H. A. Makse, "Influence maximization in complex networks through optimal percolation," Nature **524**, 65–68 (2015).
[38]J. Fan, J. Meng, J. Ludescher, X. Chen, Y. Ashkenazy, J. Kurths, S. Havlin, and H. J. Schellnhuber, "Statistical physics approaches to the complex earth system," Phys. Rep. **896**, 1–84 (2021).
[39]J. Gómez-Gardeñes, D. Soriano-Paños, and A. Arenas, "Critical regimes driven by recurrent mobility patterns of reaction–diffusion processes in networks," Nat. Phys. **14**, 391–395 (2018).
[40]J. Fan, J. Meng, Y. Ashkenazy, S. Havlin, and H. J. Schellnhuber, "Climate network percolation reveals the expansion and weakening of the tropical component under global warming," Proc. Natl. Acad. Sci. U.S.A. **115**, E12128–E12134 (2018).
[41]Y. Zou, R. V. Donner, J. F. Donges, N. Marwan, and J. Kurths, "Identifying complex periodic windows in continuous-time dynamical systems using recurrence-based methods," Chaos **20**(4), 043130 (2010).
[42]A. Bashan, R. P. Bartsch, J. W. Kantelhardt, S. Havlin, and P. C. Ivanov, "Network physiology reveals relations between network topology and physiological function," Nat. Commun. **3**, 702 (2012).
[43]C. M. Schneider, A. A. Moreira, J. S. Andrade, S. Havlin, and H. J. Herrmann, "Mitigation of malicious attacks on networks," Proc. Natl. Acad. Sci. U.S.A. **108**, 3838–3841 (2011).
[44]N. Marwan, J. F. Donges, Y. Zou, R. V. Donner, and J. Kurths, "Complex network approach for recurrence analysis of time series," Phys. Lett. A **373**, 4246–4254 (2009).
[45]Y. Zou, T. Pereira, M. Small, Z. Liu, and J. Kurths, "Basin of attraction determines hysteresis in explosive synchronization," Phys. Rev. Lett. **112**, 114102 (2014).
[46]A. A. Tsonis, K. L. Swanson, and P. J. Roebber, "What do networks have to do with climate?," Bull. Am. Meteorol. Soc. **87**, 585–596 (2006).
[47]A. A. Tsonis, K. Swanson, and S. Kravtsov, "A new dynamical mechanism for major climate shifts," Geophys. Res. Lett. **34**(13), L13705, https://doi.org/10.1029/2007GL030288 (2007).
[48]K. Yamasaki, A. Gozolchiani, and S. Havlin, "Climate networks around the globe are significantly affected by el niño," Phys. Rev. Lett. **100**, 228501 (2008).
[49]J. F. Donges, Y. Zou, N. Marwan, and J. Kurths, "Complex networks in climate dynamics," Eur. Phys. J. Special Top. **174**, 157–179 (2009).
[50]J. F. Donges, Y. Zou, N. Marwan, and J. Kurths, "The backbone of the climate network," Europhys. Lett. **87**, 48007 (2009).
[51]R. V. Donner, Y. Zou, J. F. Donges, N. Marwan, and J. Kurths, "Recurrence networks—A novel paradigm for nonlinear time series analysis," New J. Phys. **12**, 033025 (2010).
[52]D. Mukhin, A. Hannachi, T. Braun, and N. Marwan, "Revealing recurrent regimes of mid-latitude atmospheric variability using novel machine learning method," Chaos **32**(11), 113105 (2022).
[53]J. Ludescher, A. Gozolchiani, M. I. Bogachev, A. Bunde, S. Havlin, and H. J. Schellnhuber, "Improved El Niño forecasting by cooperativity detection," Proc. Natl. Acad. Sci. U.S.A. **110**, 11742–11745 (2013).
[54]N. Boers, B. Bookhagen, H. M. J. Barbosa, N. Marwan, J. Kurths, and J. A. Marengo, "Prediction of extreme floods in the eastern central Andes based on a complex networks approach," Nat. Commun. **5**, 5199 (2014).
[55]J. Meng, J. Fan, Y. Ashkenazy, A. Bunde, and S. Havlin, "Forecasting the magnitude and onset of el niño based on climate network," New J. Phys. **20**, 043036 (2018).
[56]K. Steinhaeuser, N. V. Chawla, and A. R. Ganguly, "An exploration of climate data using complex networks," in *Proceedings of the Third International Workshop on Knowledge Discovery from Sensor Data*, SensorKDD '09 (Association for Computing Machinery, New York, 2009), pp. 23–31.
[57]K. Steinhaeuser, N. V. Chawla, and A. R. Ganguly, "Complex networks as a unified framework for descriptive analysis and predictive modeling in climate science," Stat. Analysis Data Mining: ASA Data Sci. J. **4**, 497–511 (2011).
[58]M. Barreiro, A. C. Marti, and C. Masoller, "Inferring long memory processes in the climate network via ordinal pattern analysis," Chaos **21**(1), 013101 (2011).
[59]J. Deza, M. Barreiro, and C. Masoller, "Inferring interdependencies in climate networks constructed at inter-annual, intra-season and longer time scales," Eur. Phys. J. Special Top. **222**, 511–523 (2013).
[60]J. Ludescher, J. Meng, J. Fan, A. Bunde, and H. J. Schellnhuber, "Very early warning of a moderate-to-strong El Niño in 2023" arXiv:2301.10763v1.
[61]T. Liu, D. Chen, L. Yang, J. Meng, Z. Wang, J. Ludescher, J. Fan, S. Yang, D. Chen, J. Kurths, X. Chen, S. Havlin, and H. J. Schellnhuber, "Teleconnections among tipping elements in the earth system," Nat. Clim. Change **13**, 67–74 (2023).
[62]M. Jusup, P. Holme, K. Kanazawa, M. Takayasu, I. Romić, Z. Wang, S. Geček, T. Lipić, B. Podobnik, L. Wang, W. Luo, T. Klanjšček, J. Fan, S. Boccaletti, and M. Perc, "Social physics," Phys. Rep. **948**, 1–148 (2022).
[63]J. Meng, J. Fan, J. Ludescher, A. Agarwal, X. Chen, A. Bunde, J. Kurths, and H. J. Schellnhuber, "Complexity-based approach for El Niño magnitude forecasting before the spring predictability barrier," Proc. Natl. Acad. Sci. U.S.A. **117**, 177–183 (2020).
[64]J. Zhang, J. Zhou, M. Tang, H. Guo, M. Small, and Y. Zou, "Constructing ordinal partition transition networks from multivariate time series," Sci. Rep. **7**, 7795 (2017).
[65]J. Ludescher, M. Martin, N. Boers, A. Bunde, C. Ciemer, J. Fan, S. Havlin, M. Kretschmer, J. Kurths, J. Runge, V. Stolbova, E. Surovyatkina, and H. J. Schellnhuber, "Network-based forecasting of climate phenomena," Proc. Natl. Acad. Sci. U.S.A. **118**, e1922872118 (2021).
[66]X. Wang, X. Han, Z. Chen, Q. Bi, S. Guan, and Y. Zou, "Multi-scale transition network approaches for nonlinear time series analysis," Chaos, Solitons Fractals **159**, 112026 (2022).
[67]H. A. Dijkstra, E. Hernández-García, C. Masoller, and M. Barreiro, *Networks in Climate* (Cambridge University Press, 2019).
[68]J. Meng, J. Fan, Y. Ashkenazy, and S. Havlin, "Percolation framework to describe El Niño conditions," Chaos **27**(3), 035807 (2017).
[69]G. Lancaster, D. Iatsenko, A. Pidde, V. Ticcinelli, and A. Stefanovska, "Surrogate data for hypothesis testing of physical systems," Phys. Rep. **748**, 1–60 (2018).
[70]K. Fraedrich and H. Böttger, "A wavenumber-frequency analysis of the 500 mb geopotential at 50°n," J. Atmos. Sci. **35**, 745–750 (1978).
[71]E. Kalnay, M. Kanamitsu, R. Kistler, W. Collins, D. Deaven, L. Gandin, M. Iredell, S. Saha, G. White, J. Woollen, Y. Zhu, M. Chelliah, W. Ebisuzaki, W. Higgins, J. Janowiak, K. C. Mo, C. Ropelewski, J. Wang, A. Leetmaa, R. Reynolds, R. Jenne, and D. Joseph, "The NCEP/NCAR 40-year reanalysis project," Bull. Am. Meteorol. Soc. **77**, 437–472 (1996).

[72]E. K. M. Chang, "The role of wave packets in wave–mean flow interactions during southern hemisphere summer," J. Atmos. Sci. **62**, 2467–2483 (2005).
[73]T. M. Lenton, J. Rockström, O. Gaffney, S. Rahmstorf, K. Richardson, W. Steffen, and H. J. Schellnhuber, "Climate tipping points—Too risky to bet against," Nature **575**, 592–595 (2019).
[74]H. McGowan and A. Theobald, "Atypical weather patterns cause coral bleaching on the great barrier reef, australia during the 2021–2022 la niña," Sci. Rep. **13**, 6397 (2023).
[75]E. Kalnay, *et al.*, "The NCEP/NCAR 40-year reanalysis project," Bull. Am. Meteorol. Soc. **77**, 437–471 (1996).